



NRL/MR/6790--16-9706

Backward Raman Amplification in the Long-wavelength Infrared

LUKE JOHNSON
DANIEL GORDON
JOHN PALASTRO
BAHMAN HAFIZI

*Beam Physics Branch
Plasma Physics Division*

December 29, 2016

Approved for public release; distribution is unlimited.

Backward Raman Amplification in the Long-wavelength Infrared

L. A. Johnson, D. F. Gordon, J. P. Palastro, and B. Hafizi

U.S. Naval Research Laboratory, Washington, DC 20735

(Dated: November 18, 2016)

Abstract

The wealth of work in backward Raman amplification in plasma has focused on the extreme intensity limit, but backward Raman amplification may also provide an effective and practical mechanism for generating intense, broad bandwidth, long-wavelength infrared radiation. An electromagnetic finite-difference time-domain simulation coupled with a relativistic cold fluid plasma model is used to demonstrate the generation of picosecond pulses at $10\ \mu\text{m}$ with terawatt powers through backward Raman amplification. The effects of collisional and Landau damping, pump depletion, and wave breaking are examined.

CONTENTS

I. Introduction	3
II. Design Considerations	6
III. Numerical Results	9
IV. Discussion	13
V. Conclusion	14
A. Temporal Weak Coupling Gain	14
B. Collisional Damping	15
Acknowledgments	18
References	18

I. INTRODUCTION

Chirped pulse amplification has provided access to intense, few cycle, near infrared laser pulses for the last 30 years [1]. It has been proposed that backward Raman amplification could provide similar access to the multipetawatt [2] or even exawatt regime [3, 4]. While experiments have yet to reach the multipetawatt regime [5–9], it is possible that backward Raman amplification could be a practical source of long-wavelength infrared with terawatt peak powers.

The development of terawatt power pulses in the long-wavelength infrared is being driven by strong-field science, including advanced proton acceleration [10], high harmonic generation [11], mid-infrared supercontinuum generation [12, 13], and nonlinear optics [14].

There are several paths to high power long-wavelength infrared; optical parametric amplification (OPA), difference-frequency generation (DFG), optical rectification (OR), or lasing using CO₂. Frequency down-conversion from the near infrared to long-wavelength infrared is inherently inefficient. In principle, the Manley-Rowe relations limit the conversion efficiency to the ratio of the photon energies $\hbar\omega_{\text{LWIR}}/\hbar\omega_{\text{NIR}}$, about 10%. In practice, the conversion efficiency is an order of magnitude less. For example, ZnGeP₂ (ZNP) optical parametric amplifiers become inefficient beyond 5 μm [15, 16] and 10 μm [17] due to absorption [17] and group-velocity mismatch [18]. Difference-frequency generation, in combination with an optical parametric amplifier, can generate tunable broadband pulses with 10's to 100's of microjoules [19, 20], but it is limited by phase-matching and optical nonlinearities. Optical rectification in GaAs of femtosecond Ti:sapphire pulses can generate 7 μm to 20 μm [18], but is limited because optical rectification relies the pump's spectral wings [19].

Existing high power CO₂ amplifiers can create picosecond pulses with joules of energy [13, 21] at 9.4 μm and 10.6 μm . However, these amplifiers require a combination of large high pressure systems, expensive oxygen isotopes, and a high power seed pulse to sufficiently broaden the CO₂ gain spectrum for the generation of picosecond pulses. Furthermore, high gas pressure severely limits the system's repetition rate. If sufficient broadening is not achieved, these systems create pulse trains instead of individual pulses. Attempts have been made to overcome the bandwidth limitations of CO₂; one used the negative group velocity dispersion in GaAs with a beatwave to compress CO₂ laser pulse trains [13], and the other by the combination of self-chirping and a conventional dispersive compressor [22].

This suggests that a compact 10 μm source capable of terawatt powers and picosecond durations would be a key scientific and technological development. Plasma-based, backward Raman amplification can provide the bandwidth that is difficult to achieve in a CO_2 amplifier. The mechanism is self-phase-matched and optical nonlinearities in plasmas are weaker than in crystals. Additionally, the pumping CO_2 laser can be narrow-band, which removes the need for operation at high pressure, and in turn, improves the prospects for high repetition rate operation.

In backward Raman amplification, a backward propagating seed pulse, with frequency and wavenumber ($\omega_1 \approx \omega_0 - \omega_p, k_1 \approx -k_0$), stimulates the coherent backscattering of a forward propagating pump pulse (ω_0, k_0) off of a plasma (Langmuir) wave ($\omega_p, k_p \approx 2k_0$). This enhances the plasma wave and further drives the energy from the pump to seed waves leading to exponential growth in the seed energy until pump depletion or another saturation mechanism occurs [23].

This process is illustrated in FIG. 1. The pump pulse (blue) is moving in the forward direction (left-to-right) while the seed pulse (green) is moving backwards (right-to-left). A uniform plasma covers the entire region. Both, the pump and seed are linearly polarized. The seed pulse is injected once the pump pulse is overlapping the plasma, as shown in FIG. 1(a). The initial seed pulse has a full width at half maximum (FWHM) duration of 3 ps and intensity of $1 \times 10^8 \text{ W cm}^{-2}$. The seed pulse grows exponentially at the small-signal gain rate for Raman backscattering $\gamma_0 = a_0 \sqrt{\omega_0 \omega_p} / 4 = 2.20 (\lambda_0 [\mu\text{m}] I_0 [\text{W cm}^{-2}])^{1/2} (n_e [\text{cm}^{-3}])^{1/4} \text{ Hz}$, where a_0 is the pump normalized vector potential, ω_0 is the pump frequency, ω_p is the plasma frequency, λ_0 is the pump wave length, I_0 is the pump intensity, and n_e is the plasma density [23]. The results of exponential growth can be see in FIG. 1(a) as the seed intensity increased by a factor of 30 since entering the plasma. This corresponds to an approximate gain rate of $\gamma \sim 1/3.7 \text{ ps}$. During the exponential growth regime the seed pulse duration will lengthen, reaching a maximum duration of 5.2 ps in this example. This is the result of enhanced backscatter due to a build up in the plasma wave at the tail of the seed pulse. Figure 1(b) shows when the seed becomes sufficiently intense to deplete the pump. At this point, the seed is operating in the superradiant regime [24]. The leading edge of the seed is backscattering enough of the pump that it shadows the trailing edge of the seed. This results in temporal gain compression and can be see in FIG. 1(b) and 1(c), with seed durations of 3.3 ps and 1.5 ps, respectively. Figure 1(c) shows that pump depletion has

continued. The seed intensity is growing roughly linearly with propagation distance as it sweeps up the pump energy.

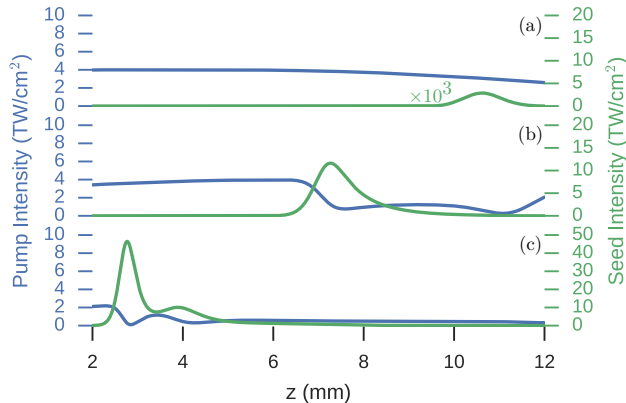


FIG. 1: The pump (blue) and seed (green) intensity at three times. (a) At $t = 97$ ps, the seed has entered the plasma and is undergoing exponential growth. (b) At $t = 110$ ps, the seed has become sufficiently intense to almost fully deplete the pump. (c) At $t = 123$ ps, the seed has continued depleting the pump while temporally compressing. The seed will continue to grow after the final frame and will reach a final seed intensity and FWHM duration of 54 TW cm^{-2} and 1.3 ps . The plasma density is $1 \times 10^{17} \text{ cm}^{-3}$.

Researchers at Princeton proposed a plasma-based approach for pulse compression that takes advantage of a nonlinear regime of amplification, superradiance, where the pulse would shorten as it grew and its intensity is proportional to the square of the number of emitters (plasma electrons) [24]. The formalism for this process was originally developed for growth from noise [25]. To access this regime, a superradiant pulse must be intense enough $\omega_B \geq \omega_p$ and short enough $\tau \approx \pi/\omega_B$, where ω_0 is the pump frequency, $\omega_B = 2\omega_0\sqrt{a_0a_1}$ is the natural frequency of an electron in a plasma wave (also called the bounce frequency), τ is the pulse duration, $a_{0,1}$ are the normalized pump and seed vector potentials, e is the electron charge, m is the electron mass, and c is the speed of light [23].

An early proposal suggested the possibility of backward Raman amplification for generating exawatt laser pulses [3] which would open access to new fundamental physical regimes [26]. In order for chirped pulse amplification to reach higher power, excessively large gratings are required to keep the laser fluence below the grating damage threshold, typically on the order of 0.1 J cm^{-2} . Plasma-based amplification avoids this issue by not using gratings

to stretch the pulse. Additionally, material damage thresholds of GW cm^{-2} are avoided by the use of a plasma instead of a crystal as a gain medium.

The critical power for relativistic self-focusing of a plasma is $P_{\text{cr}} \approx 17(\omega_0/\omega_p)^2 \text{GW}$. This is the power at which plasma nonlinearities, and instabilities, begin to become significant relative to linear effects. By having the amplification occur faster than all other instabilities, pulses above critical power could be generated. The development of the pi-pulse model dominates the theory of backward Raman amplification [3]. This uses a three-wave model to describe the pump, seed, and plasma wave. The effects of modulation instability (filamentation), wave breaking, and forward Raman scattering on amplification have been discussed at length. It was suggested that the ideal place to operate is near wave breaking and with the highest pump energy that avoids filamentation. The pi-pulse amplitude and energy should grow linearly with propagating distance. Simultaneously, the pulse duration compresses inversely proportional to propagation distance.

Three dimensional particle-in-cell simulations have been carried out which show regimes where backward Raman amplification is feasible [2]. For example, at wavelengths of 700 nm and 10 μm there are parameters that yield PW powers.

Experimentally, the observed peak output powers are 60 GW [27]. Other work has reported efficiencies of 6.4% [5] for a pump wavelength of 800 nm, seed wavelength of 890 nm, and plasma density of $1.7 \times 10^{19} \text{cm}^{-3}$.

Previous work [4] mentioned the possibility of scaling to 10 μm wavelength but for parameters where the initial seed intensity was equal to the pump intensity. While this is feasible for 800 nm, it is not for 10 μm . This makes the exponential growth regime very important to the final seed output.

II. DESIGN CONSIDERATIONS

High power, seed sources at 10 μm are lacking. Therefore, the seed must make use of both the small signal gain regime and depletion regime for backward Raman amplification to be effective. The small signal gain regime is required in order to get the seed into the depletion regime at which point a significant fraction of the pump energy can be transferred to the seed pulse.

The pump intensity and plasma density are major design considerations as both directly

influence the gain rate, wave breaking, and other instabilities. Figure 2a shows a contour plot illustrating various design limitations in this plane. The gray lines show the time-independent backward Raman gain length, the length over which the seed field strength will increase by a factor of e^1 , given by c/γ_0 , where $\gamma_0 = \sqrt{\omega_0\omega_p}a_0/4$ is the collisionless gain rate. The black lines show the effect of electron-ion collisions on the gain length c/γ , where γ is the collisional gain rate given by Eq. (A4) [23, 28]. The electron-ion collision rate depends on the plasma temperature and ponderomotive energy with a functional form approximated by $\nu_{ei} \sim (T + U_p)^{-3/2}$. While time-dependent effects are important [3], the time-independent gain rate is illustrative for understanding the trade-offs in pump intensity and plasma density.

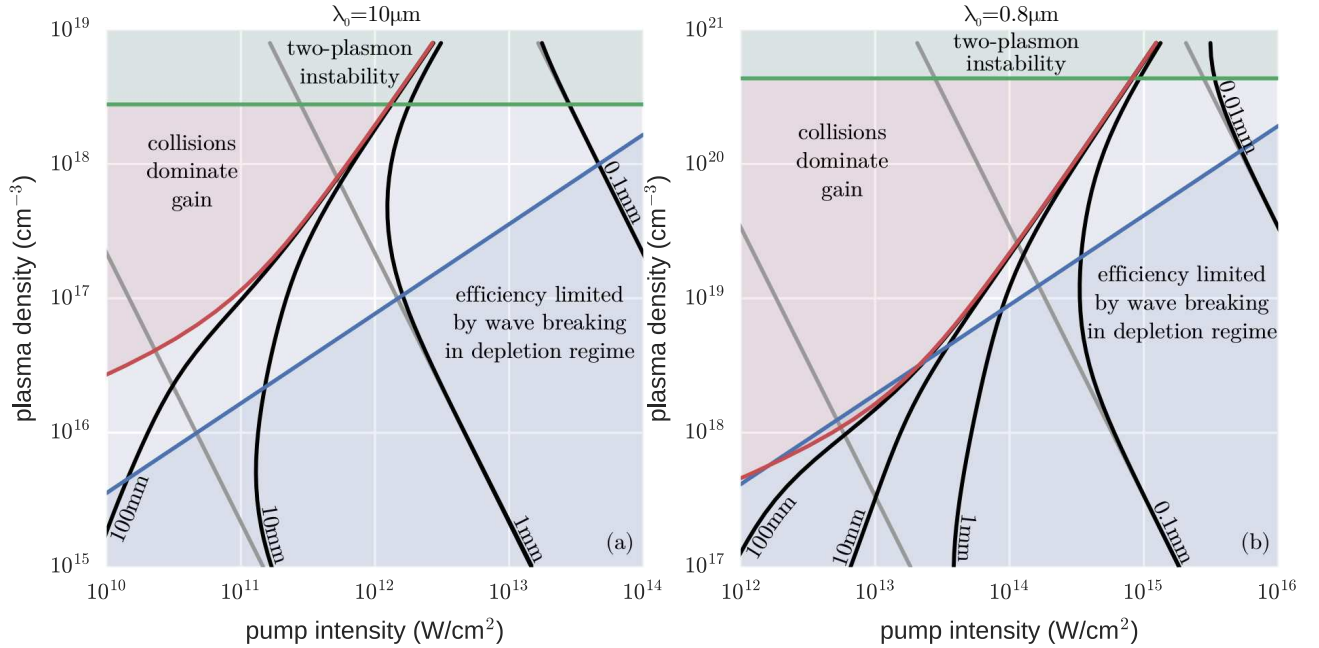


FIG. 2: Contours (black) of the steady-state Raman backscatter gain length, c/γ , are shown for 2a $\lambda_0 = 10 \mu\text{m}$ and 2b $\lambda_0 = 0.8 \mu\text{m}$. The gain length in a collisionless plasma are shown by the gray lines. The red region shows where there is no gain due to collisions $\gamma_0^2 < \nu_e \nu_s/4$. The plasma is singly ionized with temperature $T = 1 \text{ eV}$, $\ln \Lambda = 10$, $Z = 1$. The blue region shows where wave breaking would reduce the efficiency once the seed is in the depletion regime. The green region shows when two-plasmon decay would deplete the pump.

Shorter gain lengths are produced with higher pump intensities and plasma densities

because both enhance the plasma wave. At high plasma density, electron-ion collisions ($\nu_e \propto n_e$) will damp out the plasma wave faster than growth from backward Raman amplification ($\gamma_0 \propto n_e^{1/4}$) [23, 28]. The difference in the collisional and collisionless gain lengths (black and gray curves of FIGS. 2a) show where collisional damping becomes important. The red lines mark the instability threshold where the gain is zero due to collisional damping and is given by $\gamma_0^2 = \nu_e \nu_s / 4$ (see Appendix A) [23]. The isocontours of the collisional gain length (black curve) compress against the boundary where collisions dominate gain (red curve) because as the gain approaches zero, the gain length goes to infinity. Additionally, the collisional damping is suppressed relative to the nominal plasma temperature at pump intensities where the ponderomotive energy is greater than the plasma temperature $I_0 > 1.07 \times 10^{13} \text{ W cm}^{-2} T[\text{eV}] / (\lambda_0[\mu\text{m}])^2$. This can be observed in FIG. 2a when the red line changes slope.

The green line at quarter critical density $n_{\text{crit}}/4 \approx 2.8 \times 10^{20} \text{ cm}^{-3} / (\lambda[\mu\text{m}])^2$ marks where the two-plasmon decay occurs and where the Raman instability becomes absolute. This sets a hard upper bound on the possible plasma density as otherwise the pump would be rapidly absorbed by the plasma. Typically, other instabilities (forward Raman, parasitic backward Raman, or filamentation) will dominate at plasma densities below quarter critical [2].

Plasma wave breaking can limit efficient depletion of the pump. During depletion, each pump photon is stimulated to scatter into an additional seed photon and plasmon. But the plasma wave has a maximum energy density that it can support [23], in other words, a maximum plasmon density. Therefore, when the maximum plasmon density has been reached, the seed growth is stunted. Plasma wave breaking occurs when, locally, the seed has encountered a pump energy equal to the maximum-supported plasma wave energy of that region. The blue curve of FIG. 2 marks the largest pump intensity that the plasma can support during 100% depletion [29]. The pump intensity should be below $I_0 = 4.7 \times 10^{-15} \lambda_0[\mu\text{m}] (n_e[\text{cm}^{-3}])^{3/2} \text{ W cm}^{-2}$ [29] to avoid wave breaking. Plasma wave breaking does not affect the small signal growth of the seed pulse but the overall efficiency of the growth when the seed is in the depletion regime [3]. Therefore this is a soft limitation and there is evidence that some wave breaking is preferable as it can limit energy growth in the tail of the seed pulse[3].

Within these constraints, we can see the gain length varies from 10mm to 0.1mm. There are, however, experimental limitations to realizing a particular plasma length, density, and

uniformity. In particular, available sources generate long wavelength infrared pulses with microjoules of energy, requiring four to five e-foldings in the linear growth regime. The need of using both the linear and nonlinear regimes is distinct from previous studies, which focused, primarily, on near infrared or visible light where intense, short pulses for seeding are already available.

The parameter space for 10 μm can be contrasted with FIG. 2b which shows the gain length as a function of pump intensity and plasma density for 800 nm. It is clear that the operating window is smaller for 800 nm but there are not the same technological limitations on seed pulse generation.

In summary, this motivates using laser pump intensities of around $1 \times 10^{12} \text{ W cm}^{-2}$ and plasma densities around $1 \times 10^{17} \text{ cm}^{-3}$ in order to avoid, collisional damping, wave breaking, and have a gain length that is sufficiently small.

III. NUMERICAL RESULTS

Motivated by the regime described above, one and two-dimensional simulations were carried out using the turboWAVE framework which couples a finite-difference time-domain electromagnetic solver with a collisional, relativistic cold fluid plasma model [30]. The simulation domain consists of several sections in the following order; a “vacuum” section, an up ramp, a uniform plasma section, a down ramp, and a final “vacuum” section. The uniform plasma section has a density n_0 and length L_z . The “vacuum” sections have an electron density $10^{-4}n_0$. The “vacuum” and ramp sections are all 1 mm long. The electron collision model requires a constant plasma temperature and is set at 1 eV.

A scaling of the pump intensity for fixed plasma density was carried out to illustrate the effects of collisional damping, the exponential gain regime, and depletion regime on the final intensity and FWHM duration of the seed pulse. These can be seen in FIG. 3. For this specific set of simulations, the plasma density is $n_0 = 1 \times 10^{17} \text{ cm}^{-3}$, the plasma frequency is $\omega_p = 2\pi/(0.352 \text{ ps})$, the grid size is $0.01k_p^{-1}$, and the time step is $0.009\omega_p^{-1}$.

The pump pulse ($\lambda_0 = 10.6\mu\text{m}$) enters the left side of the simulation domain at $t = 0$. The initial seed pulse ($\lambda_1 = 11.8\mu\text{m}$) enters the right side of the constant plasma density region as the pump pulse at the left side reaches half its peak intensity. The seed pulse frequency was chosen to be on resonance for the Raman instability $\omega_1 = \omega_0 - \omega_p$. The

initial seed pulse's FWHM duration is 3 ps with $300 \mu\text{J cm}^{-2}$ contained within. The initial fluence was chosen so that with a 1 mm^2 cross-section, the initial seed pulse would have μJ energies. The plasma length is $L_z = 10 \text{ mm}$. The pump pulse FWHM duration is 68 ps, which corresponds to twice the plasma length $2L_z/c$.

Field values were recorded at the simulation boundaries. Spectral box filters from $\pm\omega_p/2$ around the pump and seed frequencies were used to extract individual field envelopes and intensity profiles.

Figure 3 shows the dependence of the amplified seed on pump intensity with and without electron-ion collision, the green and blue curves respectively. At intensities below $1 \times 10^{11} \text{ W cm}^{-2}$, there is no significant gain in the seed pulse because the gain length is comparable to the plasma length, as seen in FIG. 2a. As the pump intensity is increased from $1 \times 10^{11} \text{ W cm}^{-2}$ to just below $1 \times 10^{12} \text{ W cm}^{-2}$, the seed intensity in the collisionless plasma grows exponentially with pump intensity. This means that an increase in the pump intensity allows the seed to undergo additional e-foldings within the fixed plasma length. This stops at just below $1 \times 10^{12} \text{ W cm}^{-2}$, where the seed begins growing more slowly with pump intensity. The seed pulse has grown sufficiently intense that it is beginning to deplete the pump. Similar to what occurs in FIG. 1, once the seed pulse begins depleting the pump, the rate of increase in the seed intensity is no longer exponential but roughly linear with the encountered pump fluence. For fixed plasma length, this suggests that the seed will grow roughly linearly with pump intensity. The rate of increase in FIG. 3 is faster than linear, because a higher pump intensity shortens the length needed for the seed to exponentiate and reach depletion. This increases the length the seed can deplete and hence the seed grows faster than linear with pump intensity. For a pump intensity of $4 \times 10^{12} \text{ W cm}^{-2}$, the maximum seed intensity reached $5.5 \times 10^{13} \text{ W cm}^{-2}$ with a duration of 1.3 ps. However, we were not able to investigate what happens as pump intensities increase above $4 \times 10^{12} \text{ W cm}^{-2}$ because plasma wave breaking causes the fluid model to breakdown. For a 1 mm cross-sectional area, this corresponds to a peak power of 0.55 TW, energy of 0.72 J, and amplification factor of 2.4×10^5 .

The temporal dynamics of the seed pulse also show the exponential growth and depletion regimes. When the gain length is longer than the plasma length, the seed's final duration is equal to the initial duration, as seen in the first three points of FIG. 3(b). During the small signal gain regime, the point of maximal growth sweeps backwards at $c/2$ [31], essentially

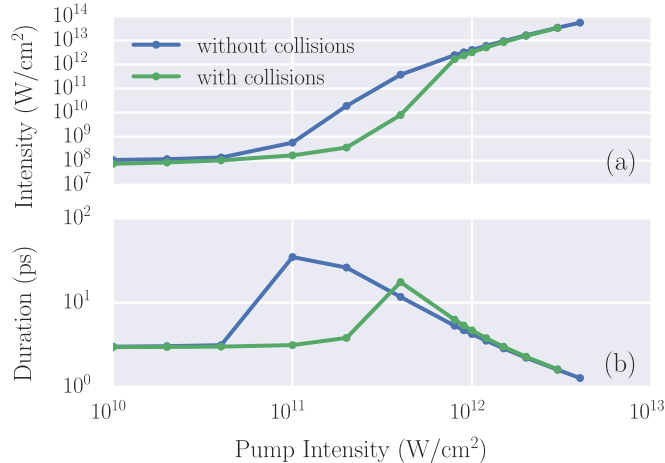


FIG. 3: The final seed (a) peak intensity and (b) FWHM duration are shown as a function of pump intensity. The blue (green) curves show the result of neglecting (including) the effect of electron-ion collisions. The maximum seed intensity reached is $5.5 \times 10^{13} \text{ W cm}^{-2}$ with a duration of 1.3 ps for a pump intensity of $4 \times 10^{12} \text{ W cm}^{-2}$.

the leading edge of the seed is driving a plasma wave so that increased backscatter will be seen later in the seed pulse. This can be seen most clearly in the collisionless plasma where seed durations of 32 ps are observed. When collisions are included, the seed duration still grows during the linearly regime but only at higher pump intensities where the electron-ion collision rate is less important. Once the seed begins depleting the pump, the seed duration rapidly decreases. What is occurring is not compression of the seed energy, but amplification in the seed's leading edge, namely temporal gain compression. Pulse durations as short as 1.3 ps are reached. This is shorter than the 2 ps-3 ps pulses that are typically created in high power CO₂ lasers [12, 22]. Previous work has shown that some degree of wave breaking is beneficial. When wave breaking occurs after the peak of the seed pulse has passed, it can suppress the growth in trailing pulses, such as those seen in FIG. 1(c) [3].

A scan of the initial pulse duration while the fluence is held fixed is shown in FIG. 4. The pump intensity is $2 \times 10^{12} \text{ W cm}^{-2}$ and all other parameters are the same as FIG. 3. There is a weak dependence of the seed's final intensity and duration on its initial duration. This is promising as it suggests that the initial seed pulse duration is not a critical design parameter.

The intensity maximum in FIG. 4(a) can be understood from the dynamics of the small signal gain. The point of maximal gain sweeps backward at half the speed of light [31]. If

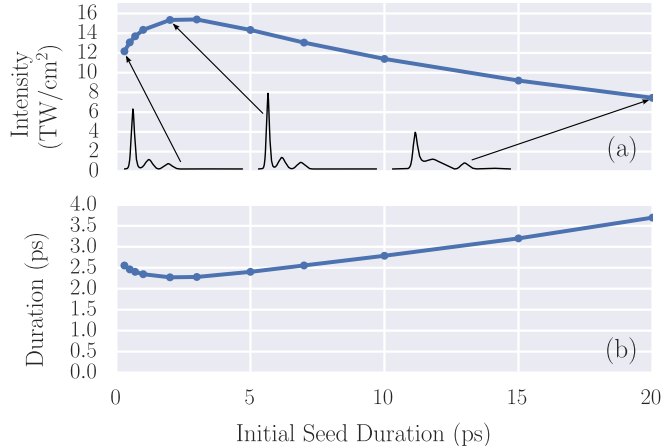


FIG. 4: The final seed (a) peak intensity and (b) FWHM duration are shown as a function of the initial seed duration. These are fluid turboWAVE simulations with electron-ion collisions. The pump intensity is 2 TW cm^{-2} , plasma density is $1 \times 10^{17} \text{ cm}^{-3}$, and plasma length is 10 mm. The black lineouts show the final intensity profiles of the seed pulse. The lineout axes cover a temporal and intensity range of 80 ps and 16 TW cm^{-2} .

the seed it too short, the point of maximal gain will pass over it and amplify the trailing tail. If the seed is too long, the head of the seed will amplify to the depletion regime before tail. In this case, the pulse would have reached depletion sooner had the pulse been shorter. The intensity profiles inset in FIG. 4(a) show this. The left intensity profile shows a short pulse on top of the amplified and temporally lengthen initial seed pulse.

Two-dimensional turboWAVE simulation results are shown in FIG. 5. This simulation is similar to the previous parameter scans with the following differences. The initial seed intensity and duration are $1 \times 10^{10} \text{ W cm}^{-2}$ and 3 ps. The pump and seed's initial e^{-1} field spot sizes are 0.4 mm. The pump intensity is $7.4 \times 10^{11} \text{ W cm}^{-2}$. The geometry is planar. The longitudinal and transverse spatial coordinates are z and x , respectively. Along the longitudinal direction, the 10 mm plasma is constructed the same as the one-dimensional simulations. The plasma profile in the transverse direction is uniform with periodic boundary conditions. The simulation domain had 83328 and 64 cells in the z - and x -directions, respectively. The cell size is $\Delta z = 0.01 k_p^{-1}$ and $\Delta x = 2 k_p^{-1}$ in the z - and x -directions, respectively.

The depletion of the pump can be seen in FIG. 5(b). The seed intensity has increased by a factor of 360. The seed has a smaller spot size due to gain focusing. This shows that

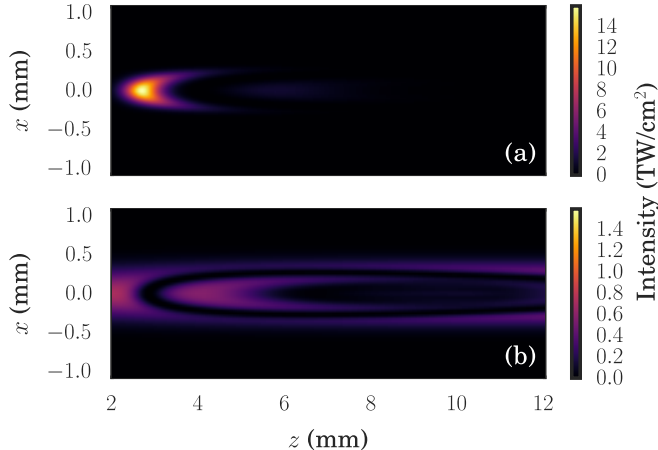


FIG. 5: Intensity of seed (a) and pump (b) just before the seed exits the plasma region.

comparable results are possible in the two-dimensional simulations in one. The transverse grid size is too large to resolve plasma perturbations needed to drive the filamentation instability. Further investigation is needed to determine the importance of that effect.

IV. DISCUSSION

Two modeling limitations have been observed when simulating backward Raman amplification. First, the fluid simulations are limited by wave breaking of the plasma. The most promising cases for amplification tend to occur when the pump intensity is at or above the wave breaking limit, as suggested by FIG. 2a and FIG. 2b. Specifically, this occurred for pump intensities of $4 \times 10^{12} \text{ W cm}^{-2}$. The pump pulse alone will not drive a significant plasma wave by itself. As the seed is amplified, it beats with the pump and drives the plasma wave to break. Fundamentally, this limits the maximum seed intensities that are possible to reach in fluid simulations at a given pump intensity.

Particle-in-cell (PIC) simulations offers the ability to model the amplification process in the regime above plasma wave breaking. Extensive PIC simulations have been carried out and show quantitative agreement with the collisionless fluid model. But when the number of potential e-foldings is sufficiently large, $\gamma_0 L_z / c \sim 4$ to 5, parasitic Raman backscatter competes with the amplification process and limits growth. The seeding of the parasitic process is several orders of magnitude larger in the PIC versus fluid simulations. This limits the use of a PIC plasma model for this problem because it is of the practical importance to

starting with an initially weak seed pulse. Detuning the interaction with a spatially varying plasma density [31] may suppress amplification of noise and make PIC simulations for these parameters more feasible, but the need of multiple e-foldings for the seed to reach depletion makes the detuning technique more challenging.

V. CONCLUSION

The turboWAVE framework has been used to carry out one and two dimensional FDTD electromagnetic simulations coupled to a relativistic cold fluid plasma model with electron collisions. Using a pump pulse that could be generated by a CO₂ laser, it was shown that a seed pulse at 11.7 μm could be amplified to $5.4 \times 10^{13} \text{ W cm}^{-2}$ and a duration of 1.3 ps. When compared to the initial pump pulse, the final seed pulse is 10 times more intense and 50 times shorter. The final seed amplification is weakly dependent on the initial seed duration which is promising as sources are limited. The ultimate limits on efficiency could not be determined because of numerical difficulties. What is needed is a collisional kinetic model in which the noise source can be controlled.

Appendix A: Temporal Weak Coupling Gain

As derived elsewhere [23, 28], the Raman backscattering dispersion relation for the plasma density perturbations with frequency ω and wavenumber \vec{k} is

$$[\omega^2 - \omega_{ek}^2 + i\nu_e\omega] \left[(\omega - \omega_0)^2 - (\vec{k} - \vec{k}_0)^2 c^2 - \omega_p^2 + i\nu_s(\omega - \omega_0) \right] = \frac{\omega_p^2 k^2 v_{os}^2}{4}, \quad (\text{A1})$$

where the Bohm-Gross frequency is $\omega_{ek}^2 = \omega_p^2 + 3k^2 v_{th}^2$, the electron thermal velocity is $v_{th} = \sqrt{T/m}$, the electron temperature is T , the energy damping rate of the electron plasma wave ν_e , the pump frequency and wavenumber are ω_0, \vec{k}_0 , the energy damping rate of the electromagnetic wave (inverse-bremsstrahlung) is $\nu_s \approx (\omega_p/\omega_0)^2 \nu_e$, and the quiver velocity is $v_{os} = eA_0/(mc)$, where the pump vector potential is $\vec{A}_L = \hat{x}A_0 \cos(k_0z - \omega_0t)$ [23].

The scattered electromagnetic wave should have a frequency $\omega_s \approx \omega_0 - \omega_p$. A frequency detuning of $\Delta\omega$ from the resonant frequency $\omega_0 - \omega_{ek}$ defines the scattered wave frequency $\omega_s = \omega_0 - \omega_{ek} + \Delta\omega$. The plasma wave should be approximately the Bohm-Gross frequency except we will define it with a real frequency shift of $\Delta\omega$ for detuning and a complex shift

of $\delta\omega$ for gain and collisional detuning, that is, $\omega = \omega_{ek} - \Delta\omega + \delta\omega$. After making the approximation that $\delta\omega, \Delta\omega \ll \omega_{ek}$ the dispersion relation reduces to

$$(\delta\omega + i\nu_s/2)(\delta\omega + i\nu_e/2 - \Delta\omega) = -\gamma_0^2, \quad (\text{A2})$$

where the resonant, collisionless gain rate is

$$\gamma_0^2 = \frac{\omega_p^2 k^2 v_{os}^2}{16\omega_{ek}(\omega_0 - \omega_{ek})}. \quad (\text{A3})$$

The complex frequency shift of the plasma density perturbation is

$$\delta\omega = -i\frac{\nu_e}{2} + i \left(\frac{\nu_e - \nu_s}{4} - i\frac{\Delta\omega}{2} + \sqrt{\gamma_0^2 + \left(\frac{\nu_e - \nu_s}{4} - i\frac{\Delta\omega}{2} \right)^2} \right). \quad (\text{A4})$$

In the limit of no collisions $\nu_e, \nu_s \rightarrow 0$ and resonant Raman $\Delta\omega \rightarrow 0$, $\delta\omega = i\gamma_0$. In the limit of resonant Raman $\Delta\omega \rightarrow 0$ but no Raman gain $\gamma_0 \rightarrow 0$, then the frequency shift just accounts for the collisional damping of the plasma wave $\delta\omega = -i\nu_e/2$. In the limit of no Raman gain $\gamma_0 \rightarrow 0$ and no collisions $\nu_e, \nu_s \rightarrow 0$, then there is no induced frequency shift $\delta\omega = 0$.

If the interaction is resonant, $\Delta\omega = 0$, then we get the following condition for an instability $\gamma_0^2 \geq \nu_e\nu_s/4$ [23]. If $\nu_e = \nu_s = 0$, then $\delta\omega = \Delta\omega/2 + i\sqrt{\gamma_0^2 - \Delta\omega^2/4}$ which says that an instability only exists for $\Delta\omega < 2\gamma_0$. The power spectrum after an interaction time of T , will be proportional to $\exp[2\sqrt{\gamma_0^2 - \Delta\omega^2/4}T]$. In the limit that the detuning is much less than the resonant, collisionless gain rate, the FWHM duration of the seed intensity will be approximately $\tau_{\text{FWHM}} = \sqrt{\ln 2T/\gamma_0}$. This says that during the linear growth regime, that the pulse durations will grow with time due to gain narrowing, and shorten with increased gain rate due to a larger gain bandwidth.

Appendix B: Collisional Damping

Collisional damping can play a significant role on backward Raman amplification depending on the pump intensity and plasma density.

The intensity-dependent electron-ion collision rate is given by $\nu_{ei} = 3\nu_0(v_{os}/2v_{th})^{-3} Q(v_{os}/2v_{th})$, where the zero intensity rate is $\nu_0 = 4\sqrt{2\pi}Z^2e^4n_e \ln \Lambda / (3m^{1/2}T^{3/2}) \approx 2.91 \times 10^{-5} n_e [\text{cm}^{-3}](T[\text{eV}])^{-3/2}\text{Hz}$, the quiver velocity is $v_{os} \approx 25.7\lambda[\mu\text{m}]\sqrt{I[\text{W cm}^{-2}]}\text{cm s}^{-1}$, the thermal velocity is $v_{th} \approx 4.19 \times 10^7 \sqrt{T[\text{eV}]} \text{cm s}^{-1}$, $Q(x) = \int_0^x dz z^2 [I_0(z^2) - I_1(z^2)] e^{-z^2}$, and

the functions $I_n(z)$ are modified Bessel functions of the first kind. The electron charge and mass are e and m . The Coulomb logarithm is $\ln \Lambda = 10$ and ionization degree is $Z = 1$. The electron-ion collision rate is proportional to the plasma density and inversely proportional to the electron velocity cubed. The thermal and quiver velocity play a role in the overall collision rate, as can be see by ν_0 and $3(v_{os}/2v_{th})^{-3}Q(v_{os}/2v_{th})$, respectively. This has been investigated in detail [32]. As laser intensity increases and the quiver velocity becomes greater than the thermal velocity, the collision rate begins to decrease.

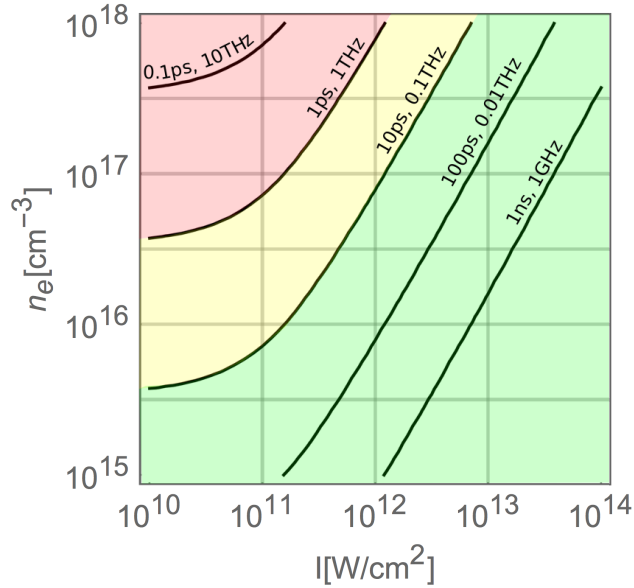


FIG. 6: The electron-ion collision time for $T = 1$ eV, $\lambda = 10$ μm , $\ln \Lambda = 10$ $Z = 1$. The green, yellow, and red regions show parameter regimes where the collision time is good, mediocre, and poor.

The effect of laser polarization on the electron-ion collision rate was estimated to not cause a difference larger than a factor of 3 in the rate [32].

Electron-neutral collisions are not considered in the simulations but are a significant consideration if the plasma is not fully ionized. The collision rate is given by $\nu_{en} = n_0 \sigma_{en} v_{th}$ where n_0 is the neutral density, $\sigma_{en} \approx 5 \times 10^{-15}$ cm^2 [33]. To include the increased rate of collisions due to electron quiver, the following substitution must be used instead of the thermal velocity alone $v_{th} \rightarrow \sqrt{v_{th}^2 + v_{os}^2}$. An approximate expression for the electron neutral collision rate is $\nu_{en} \approx 2.10 \times 10^{-7} n_0 [\text{cm}^{-3}] \sqrt{T[\text{eV}] + 3.76 \times 10^{-13} (\lambda[\mu\text{m}])^2 I [\text{W cm}^{-2}]}$. Figure 7, shows contours of constant electron-neutral collision rate. Generation of picosecond

duration pulses, requires the use of pump intensities and neutral densities where the collisional damping is slower than the seed pulse. As seen in FIG. 7, this means neutral densities below $1 \times 10^{17} \text{ cm}^{-3}$ would be feasible.

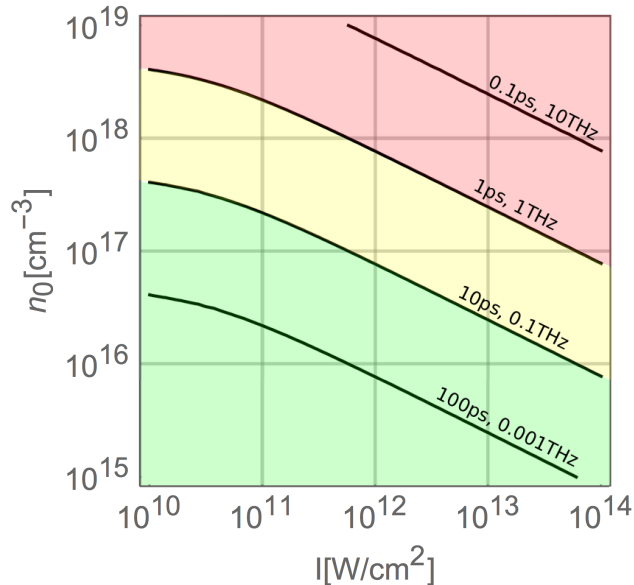


FIG. 7: The electron-neutral collision time for $T = 1 \text{ eV}$, $\lambda = 10 \mu\text{m}$, cross-section $\sigma_{en} = 5 \times 10^{-15} \text{ cm}^2$. The green, yellow, and red regions show parameter regimes where the collision time is good, mediocre, and poor relative to a 1 ps pulse duration.

Finally, previous work found evidence of Landau damping [2] but it saturated quickly and was insignificant. The damping rate can be estimated by $\delta\omega/\omega_p = -\frac{i}{2}\sqrt{\frac{\pi}{2}}(k\lambda_D)^{-3} \exp[-\frac{1}{2}(k\lambda_D)^{-2}]$ [34], where the characteristic plasma wave wavenumber is $k = 2\omega_0/c$ and the Debye length is $\lambda_D = \sqrt{T/(4\pi n_e e^2)}$. For a pump wavelength of $\lambda = 10 \mu\text{m}$, plasma density of $n_e = 1 \times 10^{17} \text{ cm}^{-3}$, temperature of $T = 1 \text{ eV}$, and $k\lambda_D = 9.33 \times 10^7 \sqrt{T[\text{eV}]/n_e[\text{cm}^{-3}]}/\lambda[\mu\text{m}] \approx 0.03$, the damping rate relative to the plasma frequency is insignificant. At lower densities of $1 \times 10^{15} \text{ cm}^{-3}$ the relative growth rate is $\text{Im}[\delta\omega]/\omega_p \sim 0.1$ and could warrant further consideration.

The units in this section are cgs-Gaussian unless otherwise stated.

ACKNOWLEDGMENTS

We would like to acknowledge Alexander Stamm for fruitful discussions on this topic. Data post-processing and plotting was carried out using the following Python packages; seaborn[35], pandas [36], numpy[37], and mpmath[38]. This work has been supported by the U.S. Naval Research Laboratory's Karle Fellowship. Resources of the Department of Defense High Performance Computing and Modernization Program (HPCMP) were used in this work.

-
- [1] D. Strickland and G. Mourou, [Optics Communications](#) **56**, 219 (1985).
 - [2] R. Trines, F. Fiuza, R. Bingham, R. Fonseca, L. Silva, R. Cairns, and P. Norreys, [Nature Physics](#) **7**, 87 (2011).
 - [3] V. Malkin, G. Shvets, and N. Fisch, [Physical Review Letters](#) **82**, 4448 (1999).
 - [4] V. Malkin, G. Shvets, and N. Fisch, [Physics of Plasmas \(1994-present\)](#) **7**, 2232 (2000).
 - [5] N. Yampolsky, N. Fisch, V. Malkin, E. Valeo, R. Lindberg, J. Wurtele, J. Ren, S. Li, A. Morozov, and S. Suckewer, [Physics of Plasmas \(1994-present\)](#) **15**, 113104 (2008).
 - [6] N. A. Yampolsky and N. J. Fisch, [Physics of Plasmas \(1994-present\)](#) **18**, 056711 (2011).
 - [7] D. Turnbull, S. Li, A. Morozov, and S. Suckewer, [Physics of Plasmas \(1994-present\)](#) **19**, 083109 (2012).
 - [8] D. Turnbull, S. Li, A. Morozov, and S. Suckewer, [Physics of Plasmas \(1994-present\)](#) **19**, 073103 (2012).
 - [9] Z. Wu, K. Zhou, X. Zheng, X. Wei, Q. Zhu, J. Su, N. Xie, Z. Jiao, H. Peng, X. Wang, *et al.*, [Laser Physics Letters](#) **13**, 105301 (2016).
 - [10] C. A. J. Palmer, N. P. Dover, I. Pogorelsky, M. Babzien, G. I. Dudnikova, M. Ispiriyan, M. N. Polyanskiy, J. Schreiber, P. Shkolnikov, V. Yakimenko, and Z. Najmudin, [Phys. Rev. Lett.](#) **106**, 014801 (2011).
 - [11] T. Popmintchev, M.-C. Chen, D. Popmintchev, P. Arpin, S. Brown, S. Ališauskas, G. Andriukaitis, T. Balčiūnas, O. D. Mücke, A. Pugzlys, *et al.*, [Science](#) **336**, 1287 (2012).
 - [12] J. Pigeon, (2014).
 - [13] J. Pigeon, S. Y. Tochitsky, and C. Joshi, [Optics letters](#) **40**, 5730 (2015).

- [14] A. Mitrofanov, A. Voronin, D. Sidorov-Biryukov, A. Pugžlys, E. Stepanov, G. Andriukaitis, T. Flöry, S. Ališauskas, A. Fedotov, A. Baltuška, *et al.*, *Scientific Reports* **5** (2015).
- [15] G. Andriukaitis, T. Balčiūnas, S. Ališauskas, A. Pugžlys, A. Baltuška, T. Popmintchev, M.-C. Chen, M. M. Murnane, and H. C. Kapteyn, *Optics letters* **36**, 2755 (2011).
- [16] G. Andriukaitis, S. Alisauskas, A. Pugžlys, A. Baltuska, L. Tan, H.-W. J. Lim, P. B. Phua, K. Balskus, and A. Michailovas, in *CLEO: Science and Innovations* (Optical Society of America, 2012) pp. CF3B–6.
- [17] A. Voronin, A. Lanin, and A. Zheltikov, *Optics Express* **24**, 23207 (2016).
- [18] G. Cerullo and S. De Silvestri, *Review of scientific instruments* **74**, 1 (2003).
- [19] A. Sell, A. Leitenstorfer, and R. Huber, *Optics Letters* **33**, 2767 (2008).
- [20] Data provided by HE-TOPAS-Prime-Plus OPA manufacturer (Light Conversion) (2016).
- [21] M. N. Polyanskiy, I. V. Pogorelsky, and V. Yakimenko, *Optics Express* **19**, 7717 (2011).
- [22] I. V. Pogorelsky, M. Babzien, I. Ben-Zvi, J. Skaritka, and M. N. Polyanskiy, *Nuclear Instruments and Methods in Physics Research Section A: Accelerators, Spectrometers, Detectors and Associated Equipment* (2015).
- [23] W. L. Kruer, *The physics of laser plasma interactions* (Reading, MA (US); Addison-Wesley Publishing Co., 1988).
- [24] G. Shvets, N. Fisch, A. Pukhov, and J. Meyer-ter Vehn, *Physical Review Letters* **81**, 4879 (1998).
- [25] G. Shvets, J. Wurtele, and B. Shadwick, *Physics of Plasmas* (1994-present) **4**, 1872 (1997).
- [26] T. Tajima and G. Mourou, *Physical Review Special Topics-Accelerators and Beams* **5**, 031301 (2002).
- [27] J. Ren, W. Cheng, S. Li, and S. Suckewer, *Nature Physics* **3**, 732 (2007).
- [28] D. J. Strozzi, *Vlasov simulations of kinetic enhancement of Raman backscatter in laser fusion plasmas*, Ph.D. thesis, Massachusetts Institute of Technology (2005).
- [29] V. Malkin and N. Fisch, *The European Physical Journal Special Topics* **223**, 1157 (2014).
- [30] D. F. Gordon, W. Mori, and T. M. Antonsen, *IEEE Transactions on Plasma Science* **28**, 1135 (2000).
- [31] V. Malkin, G. Shvets, and N. Fisch, *Physical Review Letters* **84**, 1208 (2000).
- [32] P. Catto and T. Speziale, *Physics of Fluids* (1958-1988) **20**, 167 (1977).
- [33] J. D. Huba, *NRL: Plasma formulary*, Tech. Rep. (DTIC Document, 2004).

- [34] R. Fitzpatrick, *Plasma physics: an introduction* (CRC Press, 2014).
- [35] M. Waskom, O. Botvinnik, drewokane, P. Hobson, Y. Halchenko, S. Lukauskas, J. Warmenhoven, J. B. Cole, S. Hoyer, J. Vanderplas, and et al., “seaborn: v0.7.0 (january 2016),” (2016).
- [36] W. McKinney *et al.*, in *Proceedings of the 9th Python in Science Conference*, Vol. 445 (2010) pp. 51–56.
- [37] S. Van Der Walt, S. C. Colbert, and G. Varoquaux, *Computing in Science & Engineering* **13**, 22 (2011).
- [38] F. Johansson *et al.*, *mpmath: a Python library for arbitrary-precision floating-point arithmetic (version 0.18)* (2013), <http://mpmath.org/>.